POLITECNICO DI TORINO
Repository ISTITUZIONALE

Scaling up ceramic recovery from end-of-life solid oxide cells: Process optimization and evaluation of recovered materials

Original
Scaling up ceramic recovery from end-of-life solid oxide cells: Process optimization and evaluation of recovered materials / Saffirio, S., Anelli, S., Basbus, J.F., Barbucci, A., Sabato, A.G., Smeacetto, F., Fiorilli, S.L.. - In: SUSTAINABLE MATERIALS AND TECHNOLOGIES. - ISSN 2214-9937. - ELETTRONICO. - 47:(2026), pp. 1-11. [10.1016/j.susmat.2026.e01878]

Availability:
This version is available at: 11583/3008366 since: 2026-03-09T09:19:06Z

Publisher:
Elsevier

Published
DOI:10.1016/j.susmat.2026.e01878

Terms of use:

This article is made available under terms and conditions as specified in the corresponding bibliographic description in the repository

Publisher copyright

(Article begins on next page)

19 November 2026

Sustainable Materials and Technologies 47 (2026) e01878

Contents lists available at ScienceDirect

Sustainable Materials and Technologies

journal homepage: www.elsevier.com/locate/susmat

Scaling up ceramic recovery from end-of-life solid oxide cells: Process optimization and evaluation of recovered materials

S. Saffirio [a], S. Anelli [a], J.F. Basbus [b,c,e], A. Barbucci [b], A.G. Sabato [d], F. Smeacetto [a], S.L. Fiorilli [a,*]

[a] Department of Applied Science and Technology, Politecnico di Torino, C.so Duca degli Abruzzi 24, 10129 Torino, Italy
[b] Department of Civil, Chemical and Environmental Engineering (DICCA), University of Genova (UniGe), Via All'opera Pia 15, 16145 Genoa, Italy
[c] Aragon Nanoscience and Materials Institute (INMA), Higher Council for Scientific Research (CSIC), University of Zaragoza (UniZar), C/Pedro Cerbuna 12, 50009 Zaragoza, Spain
[d] IREC- Institut de Recerca en Energia de Catalunya, Jardins de les Dones de Negre, 1, 2ª pl., 08930 Sant Adrià de Besòs, Barcelona, Spain
[e] Condensed Matter Physics Department, C/Pedro Cerbuna 12, 50009 Zaragoza, Spain

ARTICLE INFO

Keywords:
Recovered YSZ
Recovered NiO
End-of-life SOC
Scalability

ABSTRACT

This study introduces a scalable and sustainable method for recovering yttria-stabilized zirconia (YSZ) and nickel (as NiO) from end-of-life (EoL) solid oxide cells (SOCs). The process combines hydrothermal disaggregation at 200 °C with acid leaching into a single-step treatment, enabling whole-cell recycling and eliminating the need for complex layer separation. Optimised conditions – 50 g of SOC powder treated with 1 M HNO_3 for 1 h – achieved ≈92 wt% YSZ recovery while minimizing reagent use and processing time. The recovered YSZ showed a particle size distribution (445 ± 140 nm) comparable to virgin 3YSZ (470 ± 90 nm), with minimal Ni contamination (0.1 wt%) and preserved yttria content. When sintered at 1300 °C for 3 h, the material reached 95.5% relative density and an ionic conductivity of 7.9×10^{-3} S cm^{-1} at 800 °C, closely matching virgin 3YSZ (97.8%, 9.4×10^{-3} S cm^{-1}). A residual monoclinic phase (17.4 wt%), which may slightly reduce transformation toughening, did not significantly affect ionic transport. Reuse pathways for recovered YSZ include closed-loop reintegration into SOC electrolytes or supports, and open-loop valorisation such as thermal barrier coatings or catalytic substrates. Concurrently, ≈99 wt% of Ni has been recovered in the form of NiO, with Co and La contamination below 1 wt%, further supporting circular economy strategies.

1. Introduction

Yttria-stabilized zirconia (YSZ) is a widely used ceramic in high-temperature energy technologies due to its chemical, thermal, and mechanical stability. Derived from zirconium dioxide (ZrO_2) and stabilized by yttrium oxide (Y_2O_3), YSZ maintains a cubic or tetragonal structure at room temperature, suppressing the tetragonal-to-monoclinic transformation of pure zirconia [1–3]. This stabilisation enhances mechanical reliability and introduces oxygen vacancies, enabling high O^{2-} ionic conductivity at elevated temperatures [4]. Doping levels of 8–10 mol% yttria (8YSZ) result in optimal conductivity (~ 10^{-2} S cm^{-1} at 800 °C) while a lower concentration of 3 mol% yttria (3YSZ) ensures the highest material's structural integrity and mechanical strength [5]. I Among its most prominent uses is in solid oxide cells (SOCs), including fuel cells (SOFCs) and electrolysis cells (SOECs), where YSZ acts as the electrolyte, providing ionic transport with minimal electronic conductivity, ensuring chemical stability under both reducing and oxidizing atmospheres, and separating the two gas phases. Beyond SOCs, YSZ is widely employed in thermal barrier coatings (TBCs) for turbines, oxygen sensors, and catalytic converters due to its refractory nature, corrosion resistance, and thermal shock resistance [6–10].

Given its extensive application across high-performance energy systems, global demand for YSZ is expected to rise significantly in the coming years [11]. This trend is driven primarily by the deployment of SOCs, valued for high efficiency, fuel flexibility, and dual roles in hydrogen production and power generation, where YSZ can constitute over 50 wt% of the total cell mass in electrolyte- or electrode-supported designs. Its strategic importance is further reinforced by reliance on critical raw materials (CRMs), particularly yttrium, which is subject to supply risks and environmental concerns. Although zirconium has not

* Corresponding author at: Corso Duca degli Abruzzi 24, 10129 Torino, Italy.
E-mail address: sonia.fiorilli@polito.it (S.L. Fiorilli).

https://doi.org/10.1016/j.susmat.2026.e01878
Received 10 October 2025; Received in revised form 22 December 2025; Accepted 18 January 2026
Available online 22 January 2026
2214-9937/© 2026 The Authors. Published by Elsevier B.V. This is an open access article under the CC BY-NC-ND license (http://creativecommons.org/licenses/by-nc-nd/4.0/).

been formally classified as a CRM, it was included in the EU criticality assessment due to limited global supply (*Study on the EU's list of Critical Raw Materials 2020*, *Study on the Critical Raw Materials for the EU 2023*). Consequently, recycling end-of-life (EoL) SOCs and other ceramic-based components emerges as a necessary step to reduce resource dependency, mitigate environmental impacts, and support circular economy objectives [12].

State-of-the-art studies on selective YSZ recovery from end-of-life SOCs rely on separating the air-electrode layer to isolate the Ni-YSZ substrate and YSZ electrolyte, followed by acid leaching to extract metallic Ni. Various methods have been employed to remove the air electrode, including manual scraping [13,14] and ultrasonic de-coating in water [15], enabling selective recovery of Ni and YSZ without (or with very low) contamination from the air electrode. Other approaches involve soaking cells into concentrated acid after reoxidation to NiO-YSZ [16,17], removing the air electrode and allowing recovery of the NiO-YSZ composite. However, this strategy is primarily aimed at direct reuse of the composite in SOC remanufacturing, rather than selective recovery and reuse of Ni and YSZ. While effective in achieving high purity, air-electrode separation methods introduce an additional step to the process, which is particularly undesirable in selective recovery, as it already involves more steps compared to the recovery of composite NiO-YSZ. Moreover, they represent a critical bottleneck that significantly limits process scalability.

At present, robust, scalable, and simplified strategies that enable selective recovery of YSZ and Ni while minimizing process steps remain limited. A new approach was very recently proposed by Brard et al., who developed a multi-step selective leaching protocol using varying concentrations and temperatures of nitric acid to sequentially dissolve specific SOC components [18]. While promising, the method achieved recovery yields of only 60–65% for both YSZ and NiO (due to their distribution across multiple recovered products), with a high purity of 98.7% for NiO but only 95.3% for YSZ.

To address this gap, we built on our previous laboratory-scale study [13], where hydrothermal (HT) treatment in water was applied – after air-electrode removal and before acid leaching – to enhance disaggregation of Ni-YSZ composites, inspired by the pioneering work of Kamiya et al. [19] who first used HT to disaggregate pure YSZ. Here, we simplify the process by milling entire end-of-life SOCs, avoiding non-viable steps such as air-electrode scraping and powder sieving, and directly treating the powders through a combined HT–leaching process. This approach aims to simplify and streamline the recovery process, minimize material losses, maximize fragmentation of the Ni-YSZ composite to improve Ni extraction, demonstrating the scalability and feasibility of selectively recycling high-quality YSZ and Ni in a pilot reactor. Recovered YSZ is benchmarked against commercial standards for SOC reuse and, based on results, open-loop applications are also considered. The concurrent recovery of NiO further reinforces the circularity potential of the proposed recycling strategy.

2. Experimental section

2.1. Materials and equipment

SOCs supplied by Elcogen AS (Tallinn, Estonia) were used in this work. The cells feature a planar fuel-electrode-supported configuration, designed with a layered structure comprising an NiO fuel contact layer (5–10 μm), an NiO-3YSZ fuel support layer (380–390 μm), an NiO-8YSZ fuel functional layer (10–15 μm), an 8YSZ electrolyte (3–6 μm), a gadolinium-doped ceria (GDC) barrier layer (3 μm), a lanthanum strontium cobaltite (LSC) oxygen functional layer (10–15 μm) and an LSC oxygen contact layer (10–15 μm). Notably, NiO-YSZ composites constitute approximately 90% of the total mass of the SOC, highlighting their relevance in recycling strategies targeting both Ni and YSZ.

For the specific purpose of this study, EoL cells dismantled from the stack following approximately 10,000 h of operation in SOFC mode were used. Due to the reduction process occurring at the fuel-electrode side in the presence of H_2 during operation, NiO was converted into metallic Ni, resulting in Ni, Ni-3YSZ, and Ni-8YSZ layers at the end of their life (Fig. 1).

The selective recovery process previously developed at the laboratory level was here scaled-up to a large-volume BHM-2000 reactor, supplied by Berghof Products (Germany) and featuring a maximum capacity of 2 L (Fig. 2). The entire system consists of 1) the reactor – comprising an external electrical heating jacket to raise the temperature up to 200 °C and an internal stainless steel cylinder with a 2.2 L capacity, featuring a PTFE liner that reduces the effective volume to 2 L; 2) the reactor lid, equipped with valves for liquid sample extraction, a pressure relief valve with a gauge rated up to 25 bars, a rupture-disc safety system designed for pressures up to 25 bars, and an integrated manometer to monitor the internal pressure during operation; 3) a stirrer drive mounted on top of the reactor to rotate the PTFE stirrer positioned inside the chamber, ensuring uniform mixing; 4) a control unit that allows for precise programming of temperature and treatment duration for the powder suspension. N_2 is supplied from the line for sample extraction.

2.2. Recovery procedures

In contrast to the previously reported methodology [13], this approach enables the direct processing of EoL SOCs without prior mechanical separation, such as scratching or polishing, to isolate oxygen and barrier layers. These preliminary steps are indeed deemed unscalable for industrial implementation and often result in substantial material losses, particularly the complete removal of the 8YSZ electrolyte and the Ni–8YSZ fuel electrode layer. Given the relative thickness of the Ni- and YSZ-containing layers, contamination from GDC and LSC in the recovered materials is expected to be minimal and not detrimental to reuse. Therefore, the process involves fragmenting the entire cells after removing the sealant framework, milling for 6 h (as previously optimised in [13]), and direct hydrothermal treatment in the presence of HNO_3. This integrated step enables selective recovery of YSZ and Ni from the whole-cell powder, as outlined in Fig. 2.

Laboratory-scale preliminary investigations revealed partial degradation of YSZ under hydrothermal conditions at 200 °C when using a 2.2 M HNO_3 leaching solution, as employed in our previous study. These findings highlighted the need to reduce acid concentration to preserve the structural integrity of the material during recovery. As reported in detail in Section 1 of the Supplementary Information, the process of identifying the optimal set of conditions was carried out using a Design-of-Experiments approach. This allowed the influence of temperature, treatment time, acid concentration, solid-to-liquid ratio, and stirring speed to be evaluated with the aim of maximizing Ni extraction while preserving the integrity and scalability of the YSZ phase. The characterisation of the recovered materials obtained under each set of conditions included assessments of crystallinity, specific surface area, particle size, and chemical composition of the recovered powders, enabling us to determine whether the required specifications were targeted.

Based on the obtained results, the reactor-scale investigation of different treatment conditions at the reactor-scale highlighted maximum efficiency when treating 50 g of Ni-YSZ powders (s) in 1000 mL of HNO_3 1 M as liquid phase (l), resulting in s/l = 1/20, at 200 °C and with stirring fixed at 600 rpm for 1 h. Under these conditions, with a reactor filling of 50 vol%, a pressure of 5 MPa was measured using the reactor manometer. These results are detailed in **Figs. S1-S3 and Tables S1-S3**, in the **Supplementary Information (SI)**. Notably, as shown in Fig. 2, the Ni^{2+}-containing supernatant and the YSZ powders could be separately extracted from the reactor. This separation was achieved by allowing the suspended YSZ to settle during reactor cooling, followed by extraction of the supernatant through the sample valve under an inert N_2 flow. Subsequently, distilled H_2O was introduced, and stirring was applied to resuspend the deposited YSZ, producing a suspension that was eventually dried overnight.

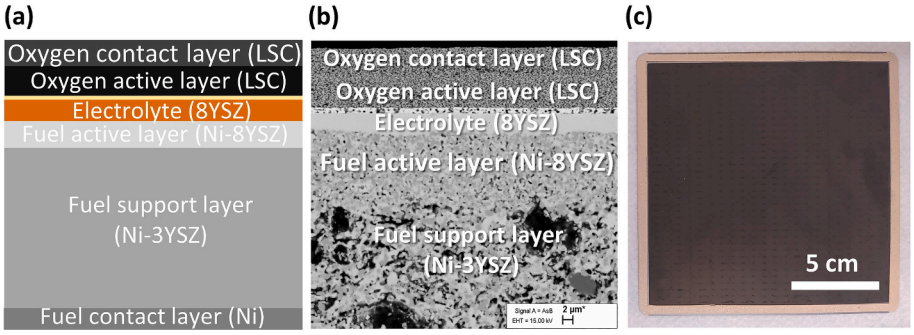


Fig. 1. Schematic representation **(a)**, polished FESEM cross-section **(b),** and digital photograph **(c)** of Elcogen fuel-electrode-supported EoL full-SOCs dismantled after stack operation in fuel mode.

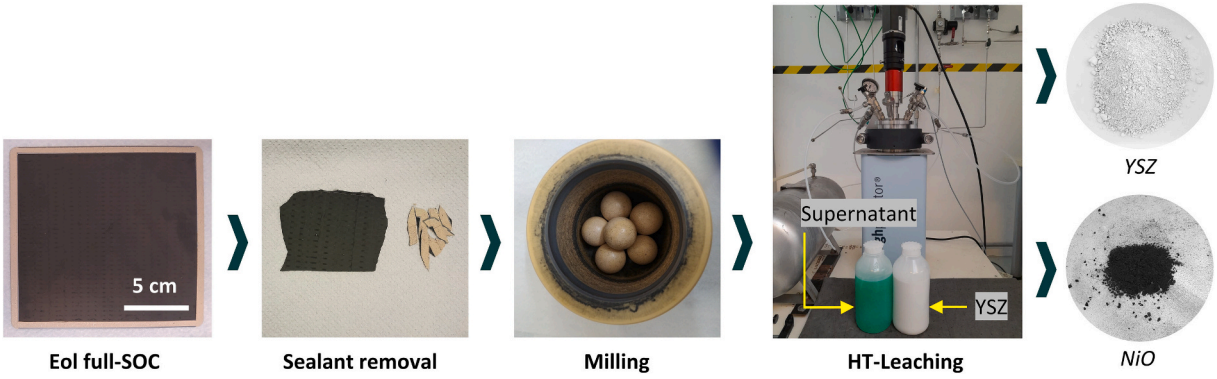


Fig. 2. Recovery of YSZ and Ni from entire EoL SOCs achieved through the direct hydrothermal treatment of the milled cell powders in the presence of HNO_3 1 M. Ni^{2+}solution is recovered as supernatant (green solution), while YSZ is recovered as white powder suspension.

The optimised conditions resulted in a remarkable improvement in the recovery process compared to the lab-scale process, reducing the s/l ratio (1/20 vs 1/50), acidic concentration (1 M vs 2.2 M), and operational time (1 h vs 4 h), thereby enhancing overall process efficiency and sustainability.

The recovered YSZ powders were rinsed with distilled water and dried overnight at 80 °C. Eventually, the recovered powder was sintered at 1300 °C for 3 h to assess the sintering ability, morphology and electrochemical performances compared to virgin 3 mol% yttria-stabilized zirconia (3YSZ).

Extracted Ni^{2+} was reprecipitated in the form of oxalate from the acid supernatants, upon addition of an excess of two times the stoichiometric amount of oxalic acid, followed by the dropwise addition of NaOH 5 M to increase the pH up to 1.00 (**SI, Section 2, Fig. S4**). The solution was stirred at 600 rpm and RT for 3 h and the resulting precipitated oxalate has been calcinated at 450 °C for 3 h to obtain NiO.

2.3. Characterisation methods

N_2 adsorption-desorption isotherm analysis was conducted using an ASAP2020 Micromeritics analyser at a temperature of −196 °C, after degassing the recovered powders at 150 °C for 4 h, to determine their specific surface area (SSA). The Brunauer–Emmett–Teller (BET) equation was used to calculate the SSA from the adsorption isotherm in the 0.04–0.2 relative pressure range.

The powders were also analysed through Dynamic Light Scattering (DLS) by use of a Zetasizer nano ZS90 (Malvern Instruments Ltd., Malvern, UK) at RT to assess their average particle size distribution (PSD). Specifically, a suspension with a concentration of powders in ddH_2O of 1 mg mL^{-1} was prepared, using sodium polymethacrylate (DARVAN) as a dispersing agent (2.5% vol.) and sonicating for 10 min before running the measurement.

Field-emission Scanning Electron Microscopy (FESEM, Jeol, JCM-6000Plus) was performed in high-vacuum conditions and at a voltage of 5 kV to evaluate the average size of the micrometric aggregates constituting the recovered powders, as well as their morphological features. Sample preparation involved immersing a steel sample holder topped with carbon tape in the powders, removing excess material using compressed air, and metallising with Pt to prevent charging effects. FESEM analysis under the same conditions was also used to morphologically characterise the recovered YSZ upon sintering at 1300 °C for 3 h, in comparison with sintered 3YSZ virgin material. In this case, both fracture surfaces and thermally etched surfaces (i.e., polished and subsequently treated at 1200 °C for 2 h) were observed to shed light on both porosity and grain morphology. Energy Dispersive Spectroscopy (EDS) was carried out at 15 kV for elemental analysis of the powders.

The sintering ability of recovered YSZ in comparison with virgin 3YSZ was determined through Hot-Stage Microscopy (HSM, Hesse Instruments, Heating microscope EM301). For the analysis, powders were pressed into small pellets and heated to 1300 °C at a rate of 5 °C min^{-1}. Each measurement was performed in triplicate for both samples.

The absolute density (g cm^{-3}) of the two materials after sintering was determined using the Archimedes method. Relative densities (%) were then calculated with respect to the reference 3YSZ theoretical value of 6.05 g cm^{-3}.

The crystallographic properties and phase composition of recovered YSZ in comparison with virgin 3YSZ were studied by X-ray Diffraction (XRD) at room temperature in air. The materials were characterised and compared both before and after sintering. PANalytical X'Pert Pro equipment with Cu Kα radiation and Bragg–Brentano geometry was operated at 40 kV and 40 mA, with an angular range (2θ) between 10° and 70°, a step size of 0.013°, a Ni filter, and a PIXcel^{1D} detector. The profiles of the XRD patterns were fitted by the Rietveld method using the FullProf Suite software, enabling to examination of the phase evolution

and structural integrity of the recovered powders. A 6th degree polynomial, Thompson–Cox–Hastings pseudo-Voigt convoluted with axial divergence asymmetry function, and isotropic Debye–Waller factors were used for the background fit, peak profiles, and atomic thermal displacement, respectively. $P4_2/nmc$ (N° 137) tetragonal (t) and $P2_1/c$ (N° 14) monoclinic (m) space groups were used as the seeds for the YSZ ceramics. For t, Wyckoff positions (WPs) for Zr/Y and O were assigned as 2b and 4d, respectively. In the case of m, Zr/Y and two O were indicated as 4e. In this sense, the weight percentage (wt%.) of t and m was obtained. Lattice parameters (a,b and c) as well as angles (β) were calculated. The crystallite size (CS) and microstrain (MS) of the powders were estimated using micrometric Y_2O_3 powders as the XRD standard, due to their larger grain size (i.e., above 5 μm) and narrower full width at half maximum (FWHM) peaks.

The concentration (wt%) of residual Ni in the recovered YSZ was evaluated by Inductively Coupled Plasma Mass Spectrometry (ICP-MS, Thermoscientific, Waltham, MA, USA, ICAP Q) after acidic digestion of the powders in concentrated HNO_3-HCl solution. In addition to quantifying residual nickel, ICP-MS analysis enabled the detection of trace contaminants originating from the oxygen electrodes, as well as the assessment of potential variations in the weight percentage of the recovered YSZ. Thermogravimetric analysis (TGA) was employed to evaluate the thermal decomposition behaviour of the oxalate, from RT up to 1000 °C at a scan rate of 5 °C min^{-1}.

The electrochemical properties of recovered YSZ and virgin 3YSZ ceramics (upon sintering) were evaluated by Electrochemical Impedance Spectroscopy (EIS) as a function of temperature. The samples were painted on both faces with platinum ink. The measurements were performed in a ProboStat device coupled with an IviumSTAT-N instrument. EIS spectra were collected between 400 and 900 °C with a step size of 50 °C, in air, with a frequency range of 1×10^6 to 0.1 Hz and an amplitude of 50 mV. In the same way, recovered YSZ was studied as a function of oxygen partial pressure (pO_2), at 800 °C. *platinum* meshes and wires were used as current collectors. EIS spectra were fitted by Zview4 software (Southern Pines, NC, USA). The total conductivity (σ_t) values were obtained by equivalent electrical circuits (EEC), which combine resistance (R) and a constant phase element (R//CPE).

3. Results and discussion

3.1. Selective recovery and characterisation of ceramic phases from EoL SOCs

3.1.1. Recovery of YSZ powder

For the recovered ceramics to be suitable for remanufacturing SOC components, the powders must meet stringent specifications in terms of chemical purity, specific surface area, and particle size distribution. The complete characterisation of the virgin commercial powder used by Elcogen for fabricating the given SOCs is available in another study by the authors [20]. SSA of 13 m^2 g^{-1} and PSD of 470 ± 90 nm were determined for virgin 3YSZ used as a benchmark for recovered materials. In the present study, as reported in Table 1, SSA and PSD of the YSZ obtained through the scaled-up and combined process, resulted in 17 m^2 g^{-1} and 445 ± 140 nm, respectively, closely matching those previously found for powder processed at lab-scale and with two distinct hydrothermal and leaching steps (17 m^2 g^{-1} and 350 ± 80 nm, respectively [13]). FESEM micrographs confirm the presence of primary nanosized particles, along with residual microaggregates averaging approximately 8 μm in size (Fig. 3).

Understanding the impact of such aggregates on the densification of YSZ upon further sintering is crucial, given reuse, as particle size plays a determinant role in the sintering ability of powders. This aspect will be investigated and discussed in the following section of this manuscript (see Section 3.2). In contrast to our previous work, where pre-sieving below 25 μm was performed to facilitate hydrothermal disaggregation, the milled powders in this study were directly processed into the HT reactor without any prior sieving. This modification resulted in notable advantages, including a significant reduction in material loss (approximately 50 wt% associated with sieving) and a decrease in overall processing time. Morphological analysis revealed that the combined hydrothermal and acid leaching treatment is highly effective in promoting disaggregation, achieving particle breakdown levels that target the reference virgin powders.

In the work firstly reported by Kamiya et al. [19], where sintered YSZ bodies were disintegrated through HT treatment, disaggregation was attributed to both the tetragonal-to-monoclinic phase transformation of YSZ and the hydrolysis of the ceramic framework at grain boundaries under hydrothermal conditions. Due to the presence of metallic Ni, the disaggregation effect was significantly hindered in the Ni–YSZ cermet recovered from SOCs, necessitating a preliminary milling step. This step was identified as the primary factor contributing to phase transformation in YSZ [13]. Therefore, the disintegration of cermet

Table 1
SSA and PSD values of YSZ recovered from treating 50 g of milled EoL SOCs through scaled-up HT-leaching treatment.

Compound	SSA (m^2 g^{-1})	PSD* (nm)
YSZ recovered from entire EoL SOCs	17	445 ± 140

* (derived from distribution % number).

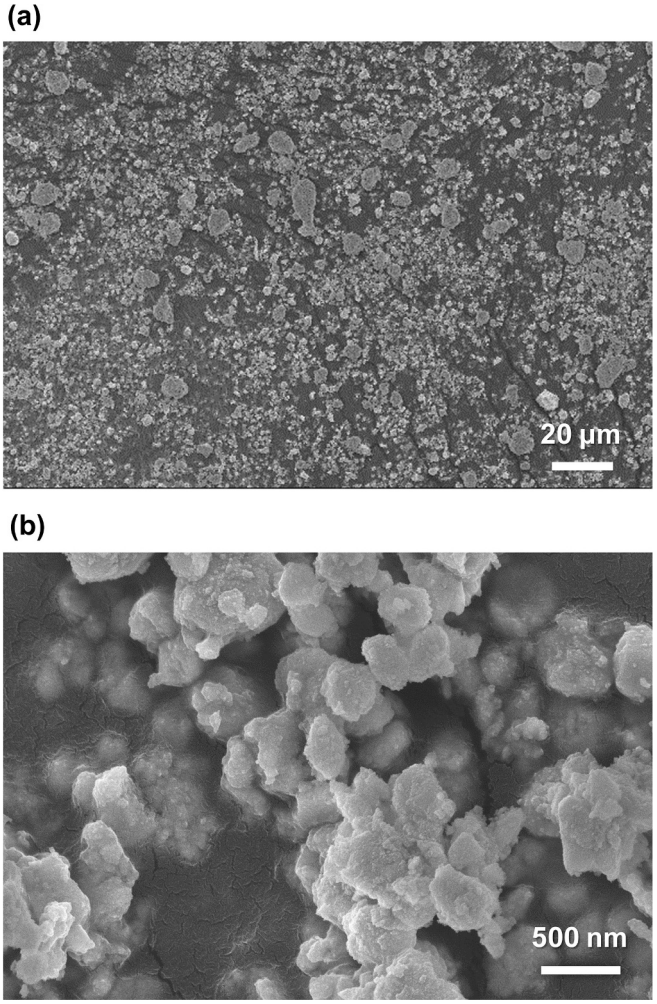


Fig. 3. FESEM micrographs at low **(a)** and high **(b)** magnification of YSZ recovered from treating 50 g of entire Eol fuel-electrode-supported SOCs through combined HT-leaching treatment at TRL5.

aggregates can be primarily attributed to the latter effect, i.e. surface hydroxylation, combined with HNO_3 oxidative leaching, which favours Ni dissolution. Hydroxylation during hydrothermal treatment of ceramics refers to the process where hydroxyl groups (–OH) are introduced or increased on the surface of ceramic materials or within their structure, during heating in an aqueous environment under pressure [21,22]. These surface groups weaken interparticle bonding, enabling the breakdown of aggregates into smaller particles [23]. In the case of YSZ, this is of particular interest, as it allows for an increase in SSA without inducing further phase transformation.

Overall, the treatment of entire EoL cells through combined HT-leaching has been demonstrated to be both feasible and effective in terms of powder characteristics.

ICP-MS analysis of the recovered YSZ powders following digestion (Table 2) revealed a residual nickel content as low as 0.1 wt%, indicating near-complete extraction of the metallic phase despite the use of low acid concentrations and short treatment durations. Visual inspection of the powders also confirmed these better outcomes, with YSZ appearing notably whiter upon combined HT-leaching (Fig. 4).

Notably, the concentrations of Zr and Y in the supernatant were negligible, indicating that no dissolution of Zr and Y occurred under the defined treatment conditions (Table 2). Results indicated the presence of 5.2 wt% Y in the recovered YSZ, corresponding to approximately 3.5 mol% Y_2O_3, a value closely matching the 3.6 mol% observed in virgin 3YSZ powders, and confirming no significant loss of Y throughout the process. Notably, no traces of Co, La or Sr, from the LSC oxygen electrode, nor Gd and Ce, from the GDC barrier layer, were detected in the recovered YSZ powders. Their exclusive presence in the supernatant confirmed their complete extraction during the process.

By directly treating the milled powders through combined HT-leaching, the overall recovery yield improved from ≈45 wt% to ≈92 wt%, demonstrating the effectiveness of adopting this simplified recycling approach. Considering a calculated ≈5 wt% loss associated with removal of the cell frame for sealant detachment, the development of a selective and scalable sealant separation method could further raise the total recovery yield to 97–98 wt%, while preserving the integrity of the electrolyte and underlying fuel-electrode layers.

LCA results from the recycling process studied here, performed with scale-up considerations by Mori et al. [24], indicate significant environmental benefits associated with material recovery and identify key process hotspots, such as energy use and material inputs. While direct cost competitiveness of recycled YSZ relative to virgin powder is not quantified in these studies, the reduced environmental burden associated with recycling suggests potential economic advantages, which merit further detailed technoeconomic analysis.

3.1.2. *Recovery of nickel in the form of NiO precipitate*

Based on the complete extraction of Ni, Co, La, Sr, Ce, and Gd observed above, the precipitation of Ni is expected to produce a mixed oxalate. Ni oxalate has been observed to precipitate at pH ≈ 1.00 (**SI, Fig. S4**), while in the literature, La oxalate is reported to begin precipitating at pH ≈ 0.70, and Co at the same pH as Ni [25]. Therefore, the presence of these elements in the supernatant is expected to affect the purity of the precipitated Ni oxalate.

Table 2
Concentration (wt%) of elements in recovered YSZ powders, and concentration (ppm) of the same elements in solution, observed after treating entire EoL cells in the large-volume reactor. Results were obtained through ICP-MS analysis (except for Y in the powders), carried out on the supernatants resulting from the digestion of YSZ powder and the supernatant recovered from the HT-leaching treatment, respectively.*

Sample	Zr	Y	Ni	Co	La	Sr	Ce	Gd
YSZ (wt%)	38.9	5.2	0.1	ND	ND	ND	ND	ND
Supernatant (ppm)	0.1	0.2	4.0×10^4	720	915	415	60	3

* Y wt% evaluated through EDS analysis (corresponding to ≈ 3.5 mol% of Y_2O_3).

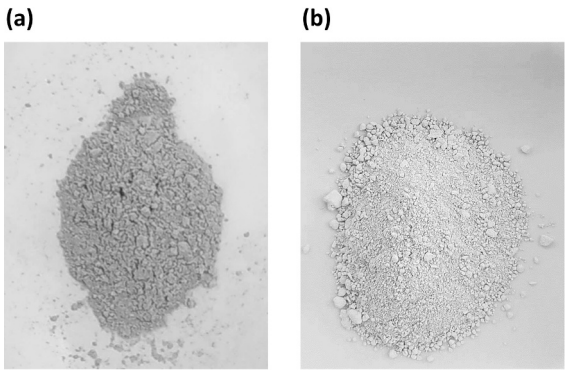


Fig. 4. Digital photographs comparing the visual aspect of the powders recovered upon separate HT and acid leaching **(a)**, and upon combined HT-leaching with the scaled-up reactor **(b)**.

TGA reveals a characteristic three-stage decomposition process of $NiC_2O_4{\cdot}2H_2O$ (**SI, Fig. S5**). A final residue of 38.7 wt% is evaluated, corresponding to 30.4 wt% of Ni and 8.3 wt% of O if assumed as pure NiO. The decomposition curve being identical to that of pure nickel oxalate, suggests that the concentrations of other metal oxalates are too low for detection through TGA. For the same reason, oxalate of elements other than Ni cannot be detected by XRD (Fig. 5 **(a)**).

A quantitative evaluation of trace contaminants in the precipitate has therefore been assessed via ICP, upon digestion of the oxalate (Table 3). Results reveal the presence of 1.1 wt% Co, 0.8 wt% La, 0.2 wt % Sr, and < 0.1 wt% for both Y and Gd, indicating that the Ni oxalate recovered from entire EoL SOCs contains non-negligible impurities, especially Co and La from the LSC oxygen layer. Depending on the intended reuse application, additional purification strategies may be required. One such approach is solvent extraction, which leverages the differential solubility of metals in two immiscible liquid phases, enabling the selective transfer of the target metal into the organic phase, followed by stripping and precipitation. Several studies have demonstrated the selective extraction of nickel from mixed-metal leachates [26,27]. However, this method necessitates carefully chosen solvents, multiple extraction stages, and precise control over phase separation and solvent recovery [28]. Alternatively, reuse applications where the presence of residual contaminants does not compromise performance should also be considered, including for example the reuse of mixed metal precursors for manufacturing mixed oxide catalysts [26–29] and battery cathodes [30–34].

Overall, the Ni content determined via ICP is in good agreement with the TGA calculation. Moreover, the negligible amount of Y detected in the precipitate confirms the full retention of the YSZ phase.

Following calcination at 450 °C for 3 h, $NiC_2O_4{\cdot}H_2O$ is converted into NiO, accompanied by particle size reduction, as evidenced by PSD values (Table 4). The resulting NiO consists of nanosized particles (450 ± 100 nm), which is consistent with the reference values for virgin NiO (630 ± 160 nm [20]), alongside microsized aggregates (2–5 μm). To optimise these powders for SOC manufacturing, milling is recommended to achieve a narrower particle size and reduce large aggregates, which could otherwise impact microstructure stability and mechanical properties [35–37]. The complete conversion of the dihydrate oxalate into the oxide was confirmed, yielding an XRD diffraction pattern equivalent to that of the commercial virgin NiO (Fig. 5 **(b)**). An overall Ni recovery of 99% was achieved.

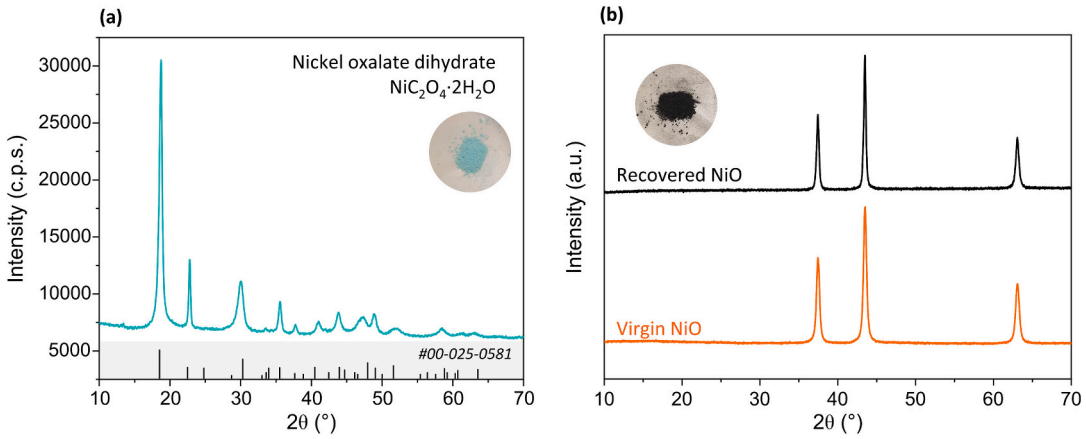


Fig. 5. XRD analyses of the nickel oxalate dihydrate precipitated at pH 1.00 from the supernatants recovered after treating the entire EoL SOCs in the large-volume reactor **(a),** and of the resulting nickel oxide obtained upon calcination, benchmarked against the virgin reference powder **(b)**.

Table 3
Concentration (wt%) of Ni and trace contaminants – originating from the Ni-YSZ fuel electrode, YSZ electrolyte, GDC barrier layer, and LSC oxygen electrode – in the oxalate precipitated at pH 1.00 from the supernatant following treatment of the entire EoL SOCs in the large-volume reactor.

Ni (wt%)	Co (wt%)	La (wt%)	Sr (wt%)	Y (wt%)	Zr (wt%)	Ce (wt%)	Gd (wt%)
31.9	1.1	0.8	0.2	<0.1	ND*	ND*	< 0.1

* ND = not detected.

Table 4
PSD values of the $NiC_2O_4·2H_2O$ powders obtained after precipitation and of the NiO powders derived from their calcination, in comparison with virgin NiO.

Compound	PSD* (nm)
Recovered $NiC_2O_4·H_2O$	550 ± 150
Recovered NiO	450 ± 100
Virgin NiO	630 ± 600

* (derived from distribution % number).

3.2. Characteristics and performances of recovered YSZ upon reprocessing

The reuse potential of recovered YSZ for closed-loop recycling, where materials are reintegrated into the production of new SOC components, was assessed through comprehensive characterisation of the powder following sintering treatment.

XRD results of both recovered YSZ and virgin 3YSZ, before and after sintering, are shown in Fig. 6(a), supported by Rietveld refinement (Fig. 6(b)). Phase composition (wt%), CS (nm) and MS (%%) are summarized in Table 5, while lattice parameters are reported in Table 6.

As previously reported, the recovery multistep process – particularly the high-energy milling step – was found to induce a pronounced tetragonal-to-monoclinic phase transformation in the YSZ component when compared to both virgin 3YSZ powders and the starting Ni-YSZ EoL materials. This transformation was qualitatively inferred from the increased relative intensity of monoclinic diffraction peaks. Here, through quantitative Rietveld refinement performed on the XRD data of the powders, the monoclinic phase content is determined to be 43.3 wt %, significantly higher than the 30.7 wt% measured in the virgin reference powders (Table 5). Notably, following sintering at 1300 °C for 3 h, virgin 3YSZ undergoes complete stabilisation into the tetragonal phase (100 wt%), whereas the recovered powders reach 82.6 wt%,

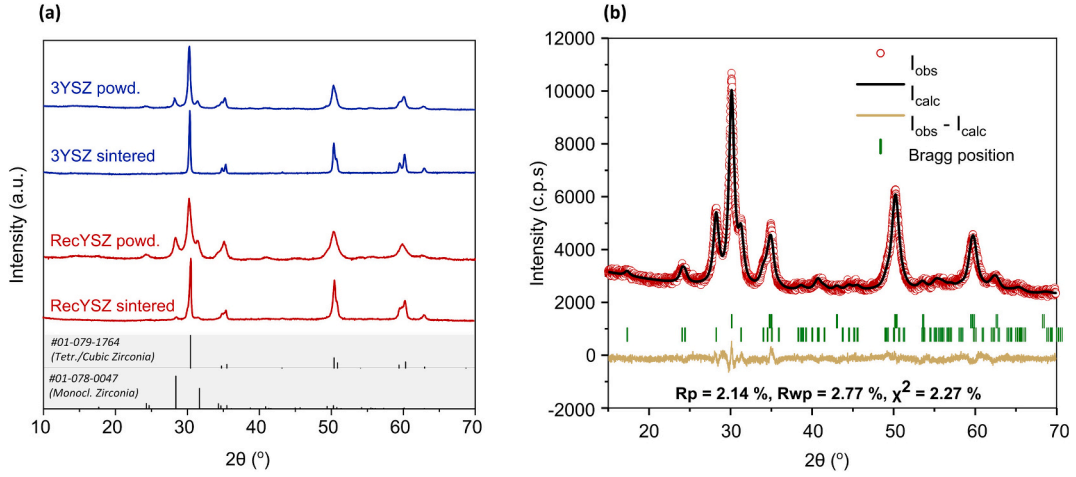


Fig. 6. (a) XRD analyses of recovered YSZ powders (red) upon sintering, in comparison with reference virgin powders of commercial 3YSZ (blue) provided by Elcogen and sintered under the same conditions. **(b)** Rietveld refinement of recovered YSZ is shown as representative for the refinement of all the samples: the intensity (I) is expressed in counts per second (c.p.s.); observed I (I_{obs}), calculated I (I_{calc}), difference between both (I_{obs} - I_{calc}), and Bragg positions are indicated above, along with the goodness of fit parameters as profile factor (Rp), weighted profile factor (Rwp) and chi-square (χ^2) below. (For interpretation of the references to color in this figure legend, the reader is referred to the web version of this article.)

Table 5
Phase composition (wt%) and microstructural parameters (i.e. crystallite size CS (nm) and microstrain MS (%%)) obtained by the Rietveld method for virgin 3YSZ and recovered YSZ powders before and after sintering.

Sample	Phase composition (wt%)		Microstructural parameters			
	t	m	t		m	
			CS (nm)	MS (%%)	CS (nm)	MS (%%)
Virgin 3YSZ_powder	69.3 ± 0.04	30.7 ± 0.04	32.5 ± 0.01	20.7 ± 0.01	13.8 ± 0.01	14.8 ± 0.01
RecYSZ_powder	56.8 ± 0.04	43.3 ± 0.05	10.3 ± 0.01	40.5 ± 0.01	10.2 ± 0.01	46.6 ± 0.01
Virgin 3YSZ_sintered	100	–	–	<10	–	–
RecYSZ_sintered	82.6 ± 0.07	17.4 ± 0.06	51.1 ± 0.01	14.7 ± 0.01	16.0 ± 0.01	35.2 ± 0.01

Table 6
Lattice parameters (**Å**) and angles (°) obtained from the Rietveld method for virgin 3YSZ and recovered YSZ samples before and after sintering at 1300 °C for 3 h.

Sample	Phase					
	t		m			
	a = b (Å)	c (Å)	a (Å)	b (Å)	c (Å)	β (°)
Virgin 3YSZ_powder	3.610 ± 0.001	5.172 ± 0.001	5.169 ± 0.001	5.207 ± 0.001	5.323 ± 0.001	98.86 ± 0.01
RecYSZ_powder	3.625 ± 0.001	5.160 ± 0.002	5.178 ± 0.001	5.196 ± 0.001	5.332 ± 0.001	98.63 ± 0.01
Virgin 3YSZ_sintered	3.608 ± 0.001	5.173 ± 0.001	–	–	–	–
RecYSZ_sintered	3.613 ± 0.001	5.176 ± 0.001	5.200 ± 0.004	5.154 ± 0.004	5.326 ± 0.003	98.82 ± 0.04

indicating the persistence of a monoclinic fraction.

The presence of the monoclinic fraction could be due to either an incomplete reversion to the tetragonal phase during sintering or a further t-m transformation during cooling, with possible implications for the mechanical performance and ionic conductivity of the recycled YSZ. From a mechanical standpoint, it may hinder the material's ability to benefit from transformation toughening, a mechanism that enhances fracture toughness in partially stabilized zirconia ceramics through stress-induced phase transitions [38]. Since mechanical robustness is critical for SOC components subjected to thermal cycling and mechanical stress during operation, this limitation could pose a barrier to closed-loop recycling applications where structural integrity is essential. From an ionic conduction perspective, instead, the influence may arise from the different crystal structures and vacancy concentrations. Indeed, while in the monoclinic phase each Zr ion is typically seven-fold coordinated with oxygen ions, tetragonal zirconia is stabilized upon partial substitution of Zr^{4+} ions with Y^{3+} ions, leading to the formation of O^{2-} vacancies to preserve charge neutrality [39]. The result is an enhanced ionic conductivity compared to the monoclinic phase, which is even more pronounced in the cubic phase.

Notably, chemical analyses in the previous result section showed no significant leaching of Y during the recovery treatment, ruling out yttria deficiency as the primary cause of this incomplete tetragonal stabilisation. Therefore, the persistence of the monoclinic phase post-sintering cannot be attributed to insufficient dopant concentration for phase stabilisation. Alternative explanations must be considered, such as the presence of microstructural defects due to inhomogeneous powder packing [40], thermal ageing effects inherited from the SOC's operational history [41], or stress fields induced by the recovery process itself. In this regard, microstrain evaluated through Rietveld analysis (Table 5) reveals a more pronounced lattice deformation in the recovered YSZ compared to the virgin 3YSZ, both in powder and sintered forms. Optimised thermal profiles, post-processing steps or compositional control are potential corrective strategies that could enhance the phase purity and, consequently, the functional properties of the recycled YSZ according to the desired application. Further investigation in this direction is warranted to unlock the full potential of reuse scenarios.

Visual evaluation and microstructural analysis (Fig. 7), along with HSM characterisation (Fig. 8) of the powders, reveal a different sintering ability for the two materials. A photographic comparison of sintered pellets revealed a reduction in shrinkage in the recovered samples, despite the starting pellets being of identical size and mass. This outcome is corroborated by HSM measurements, which highlight a corresponding decrease in shrinkage extent. The reduced sintering activity of recovered YSZ can be attributed to the thermal history undergone during SOC manufacturing and operation. Indeed, exposure to high temperatures during fabrication and service may lead to partial grain coarsening or sintering at the microstructural level, which in turn hinders further densification during post-recovery thermal treatment. Additionally, the presence of sintered micro-aggregates within the recycled powder likely impairs uniform sintering, thereby contributing to the reduced shrinkage behaviour observed upon reuse.

Further FESEM images of fracture surfaces support these findings, revealing increased porosity in the recovered samples (Fig. 7). Quantitatively, the recovered YSZ has achieved a relative density value of 95.5%, which is slightly lower than the 97.8% measured for the virgin counterpart (Table 7). Despite this reduced densification, the achieved density still indicates a relatively high sintering ability, particularly for a recycled ceramic that has undergone extensive thermal cycling. It should be noted that the sintering behaviour discussed here refers to monolithic YSZ pellets and therefore represents a conservative scenario. In practical SOC anode supports, YSZ is combined with NiO in a composite structure, and – considering a targeted reuse rate of 30% of the YSZ fraction – the recovered YSZ would account for only about 15 wt% of the total support mass. A comprehensive evaluation of co-sintering behaviour in realistic multilayer SOC architectures, accounting for powder characteristics, sintering conditions, and the fraction of recycled YSZ, will be required to fully assess shrinkage matching and cell-level integration and is identified as an important direction for future work.

Concurrent microstructural analysis of fracture surfaces at higher magnification evidences aggregates and coarser grains in the recovered material of ≈ 320 nm for the sample prepared with virgin 3YSZ powders, while the recovered sample shows slightly coarser grains, approximately ≈ 420 nm. Thermally etched surfaces clarify that these aggregates are composed of fine crystallites comparable in size to those of virgin YSZ. These observations are consistent with the CS values obtained through Rietveld refinement (Table 5), confirming that, although some morphological differences emerged, the fundamental building blocks of the material remained nearly unchanged in size.

From a functional standpoint, ionic conductivity results assessed via EIS offer promising results. Representative Nyquist plots at 600, 700 and 800 °C for recovered YSZ after sintering are shown in Fig. 9(a), while a plot of the ln of conductivity (σ) vs 1000/T in the range between 400 and 900 °C is shown in Fig. 9(b) for both recovered YSZ and virgin 3YSZ.

Notably, both virgin and recovered YSZ exhibited comparable performance, with the recovered material achieving a total ionic conductivity of 7.9×10^{-3} S cm^{-1} at 800 °C, closely matching the 9.4×10^{-3} S cm^{-1} of the virgin YSZ at the same temperature. The activation energies (E_a) values are also similar, measuring 0.91 ± 0.01 eV and 0.88 ± 0.01 eV, respectively (Table 8). These findings suggest that, despite the increased porosity and residual monoclinic phase content, the recovered material retains a robust ionic transport capability. This is a critical

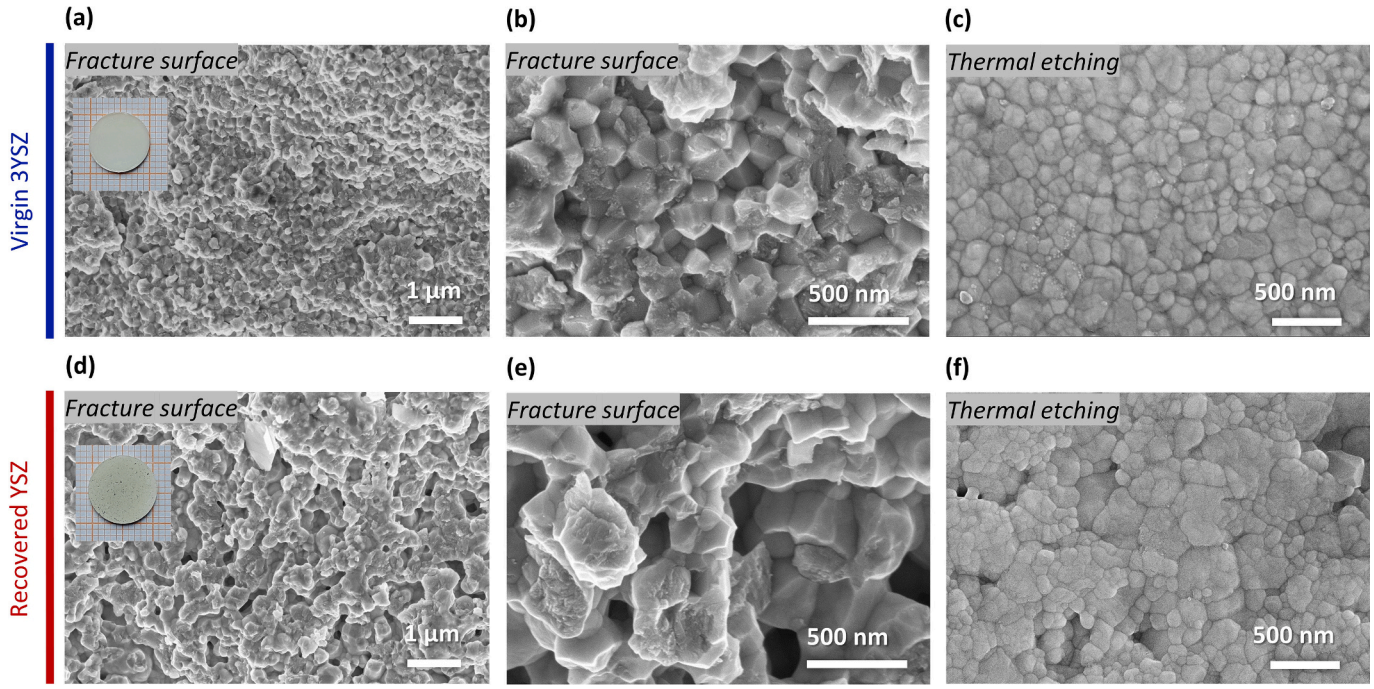


Fig. 7. FESEM micrographs of virgin 3YSZ (blue) and recovered YSZ (red) showing their fracture surfaces at low magnifications (**a** and **d**, respectively), fracture surfaces at high magnifications (**b** and **e**, respectively) and thermally-etched surfaces (**c** and **f**, respectively) upon sintering. A digital photograph of the corresponding pellets is shown above the micrographs at low magnifications, evidencing the different shrinkage extents of the two materials after the thermal treatment. (For interpretation of the references to color in this figure legend, the reader is referred to the web version of this article.)

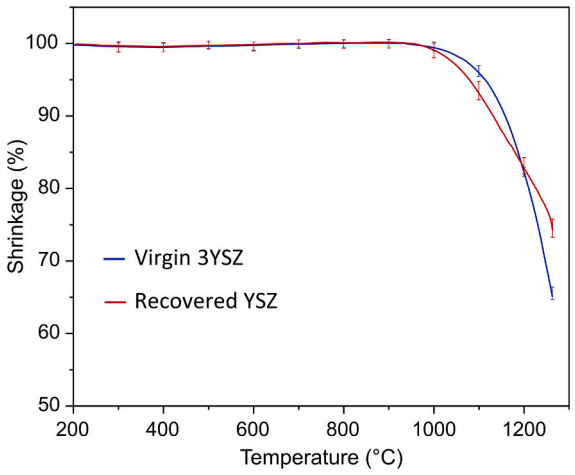


Fig. 8. Comparison of the shrinkage behaviour of virgin 3YSZ (blue) and recovered YSZ (red) powders upon heating. (For interpretation of the references to color in this figure legend, the reader is referred to the web version of this article.)

Table 7
Archimedes density (g cm^{-3}) and relative density (%) values obtained for virgin 3YSZ and recovered YSZ powders upon sintering.

Sample	Archimedes density (g cm^{-3})	Relative density (%)
Virgin 3YSZ	5.92	97.8
Recovered YSZ	5.78	95.5

criterion for closed-loop recycling into SOCs, where oxide-ion conductivity is the primary functional property required for the electrolyte or electrolyte-supporting substrates.

Table 8
Total conductivity values (S cm^{-1}) at 800 °C and E_a values (eV) of virgin 3YSZ and recovered YSZ, both sintered at 1300 °C for 3 h.

Sample	Ionic conductivity at 800 °C (S cm^{-1})	E_a (eV)
Virgin 3YSZ	9.4×10^{-3}	0.88
Recovered YSZ	7.9×10^{-3}	0.91

Despite the minimal residual amount of Ni (0.1 wt%), conductivity tests were extended to various atmospheres to exclude its potential electronic contribution to the total conductivity evaluated above. Specifically, tests were performed ranging from oxidizing (100% O_2) to reducing (100% H_2) environments at a stable temperature of 800 °C, with an intermediate step in inert conditions (100% N_2). Under reducing conditions, NiO, formed from residual Ni during sintering in air, is reduced to metallic Ni, enabling the detection of its possible contribution to electronic conduction. The results, presented in Fig. 10 as a logarithmic plot of conductivity versus oxygen partial pressure, show a slight increase in conductivity upon reduction: from 7.7×10^{-3} S cm^{-1} in 100% O_2, to 8.7×10^{-3} S cm^{-1} and 8.5×10^{-3} S cm^{-1} in 10% and 100% H_2, respectively. Though this variation may appear significant on a logarithmic scale, the absolute change was minimal and within expectations for stabilized zirconia exposed to reducing environments. Indeed, literature reports indicate that stabilized zirconia remains an excellent oxide-ion conductor and an electronic insulator under most conditions [42], but applications of small bias voltage or deviations in pO_2 can induce n-type conductivity through the generation of oxygen vacancies [43,44]. In particular, at decreasing pO_2 values, the concentration of oxygen vacancies increases, leading to the formation of more negatively charged oxygen vacancies and a transition from a prevalent p-type to an n-type conductivity [45]. For reference, an electrical contribution of about 1×10^{-3} S cm^{-1} was observed for Gd/Ce-doped 3YSZ [46] and Y-doped Ce-stabilized ZrO_2 [47], with an Electrolytic Domain Boundary (EDB) of about 10^{-16} and 10^{-12} atm, respectively, at

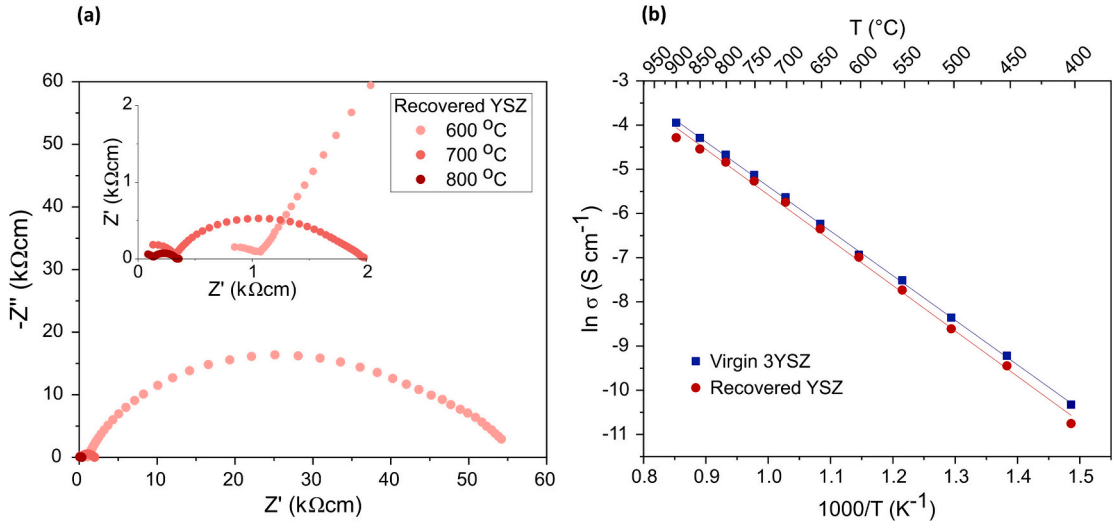


Fig. 9. Representative Nyquist plots at 600, 700 and 800 °C for recovered YSZ after sintering **(a)**; plot of the ln of conductivity (σ) vs 1000/T showing the total ionic conductivity in the 400–900 °C temperature range of both virgin 3YSZ (blue) and recovered YSZ (red) upon sintering **(b)**. (For interpretation of the references to color in this figure legend, the reader is referred to the web version of this article.)

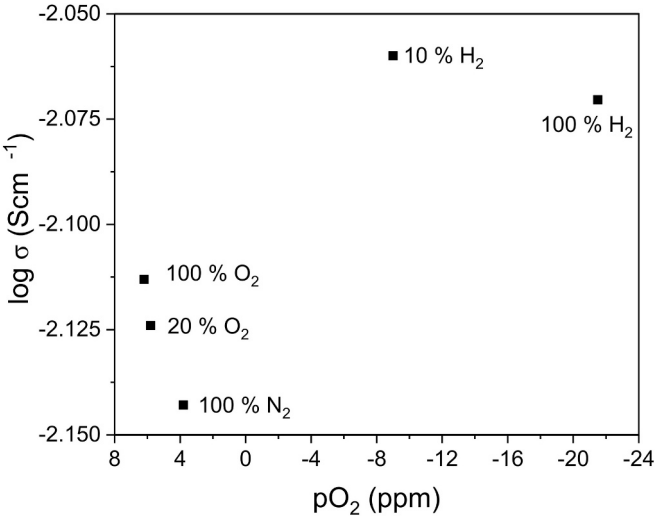


Fig. 10. Total conductivity at 800 °C of recovered YSZ as a function of O_2 partial pressure (pO_2), accounting for both ionic and electronic contributions.

800 °C. EDB is the value of pO_2 where the electronic conductivity begins to overwhelm the ionic conductivity. Therefore, the trends observed in this study align with this known behaviour, and the minimal change in conductivity is not ascribable to the presence of residual Ni (0.1 wt%).

Future works should address the mechanical characterisation of NiO/YSZ supports containing recycled YSZ, as well as single-cell fabrication and performance testing, to fully assess the effects of powder characteristics, microstructure, and recycled YSZ fraction on SOC performance and durability.

4. Conclusions

This study demonstrates a simplified and scalable process for the recovery and reuse of yttria-stabilized zirconia (YSZ) from end-of-life solid oxide cells, building upon previous small-scale work by significantly improving process efficiency and recovery yield. The combined hydrothermal–leaching treatment enables a reduction in acid concentration (from 2 to 1 M HNO_3) and treatment time (from 4 to 1 h), while increasing solid loading (from 20 to 50 g L^{-1}) and raising the overall YSZ recovery yield from 45 to 92 wt% without the need for powder sieving. Residual nickel content in the recovered powder was reduced to 0.1 wt %, which was shown not to affect the insulating behaviour of YSZ based on conductivity measurements under different atmospheres.

Despite a slightly reduced sintering activity, the recovered YSZ retains high relative density (95.5%) and ionic conductivity (7.9×10^{-3} S cm^{-1}), comparable to those of virgin 3YSZ (97.8% and 9.4×10^{-3} S cm^{-1}, respectively), confirming its functional suitability for reuse. This demonstrates the potential for selective recycling that preserves material performance, allowing integration in closed-loop SOC applications or in open-loop roles such as catalytic supports, structural ceramics, or thermal barrier materials. A careful evaluation of mechanical properties remains necessary for applications requiring high fracture toughness, such as support electrodes.

Life cycle assessment performed with scale-up considerations indicates significant environmental benefits of the proposed recycling route, reinforcing its relevance for circular material strategies. Overall, this work provides a robust materials-level validation, showing that simplified and scalable selective recycling can efficiently recover high-quality YSZ concurrently to NiO, offering a clear pathway for industrial implementation and future investigations into mechanical properties, single-cell performance, and techno-economic optimization.

CRediT authorship contribution statement

S. Saffirio: Writing – review & editing, Writing – original draft, Visualization, Validation, Methodology, Formal analysis, Data curation, Conceptualization. **S. Anelli:** Writing – review & editing, Validation, Data curation. **J.F. Basbus:** Writing – original draft, Validation, Methodology, Investigation, Data curation. **A. Barbucci:** Writing – review & editing, Methodology. **A.G. Sabato:** Writing – review & editing, Validation, Methodology. **F. Smeacetto:** Writing – review & editing, Funding acquisition, Data curation. **S.L. Fiorilli:** Writing – review & editing, Supervision, Resources, Funding acquisition, Conceptualization.

Declaration of competing interest

The authors declare that they have no known competing financial interests or personal relationships that could have appeared to influence the work reported in this paper.

Acknowledgements

Dr. A.G. Sabato would like to acknowledge Ramon y Cajal fellowship (RYC2021–034470-I, funded by MCIU/AEI/10.13039/501100011033 and by European Union NextGenerationEU»/PRTR).

This work is partially supported by the HyP3D (Hydrogen Production in Pressurized 3D-Printed Solid Oxide Electrolysis Stacks) project, funded by the European Union (Grant Agreement No. 101101274) and by the DESIREE (DEvelopment of enhanced SOEC components for Improved REliability Endurance) project, funded by the European Union (Grant Agreement No. 101251323). Views and opinions expressed are however those of the author(s) only and do not necessarily reflect those of the European Union or Clean Hydrogen Joint Undertaking. Neither the European Union nor the granting authority can be held responsible for them.

Appendix A. Supplementary data

Supplementary data to this article can be found online at https://doi.org/10.1016/j.susmat.2026.e01878.

Data availability

Data will be made available on request.

References

[1] A. Arafati, E. Borhani, S.M.S. Nourbakhsh, H. Abdoos, Synthesis and characterization of tetragonal / monoclinic mixed phases nanozirconia powders, Ceram. Int. 45 (2019) 12975–12982, https://doi.org/10.1016/j.ceramint.2019.03.225.

[2] X. Song, Y. Ding, J. Zhang, C. Jiang, Z. Liu, C. Lin, W. Zheng, Y. Zeng, Thermophysical and mechanical properties of cubic, tetragonal and monoclinic ZrO2, J. Mater. Res. Technol. 23 (2023) 648–655, https://doi.org/10.1016/j.jmrt.2023.01.040.

[3] A. King, Mitigating criticality, part III: Improving the stewardship of existing supplies, in: Yttria Stabilized Zirconia - an Overview, 2021. ScienceDirect Topics. accessed on 9 May 2025. Available online: https://www.sciencedirect.com/topics/materials-science/yttria-stabilized-zirconia.

[4] J.W. Martin, 4 - Glasses and ceramics, in: J.W. Martin (Ed.), Materials for Engineering (Third Edition), Woodhead Publishing, 2006, pp. 133–158.

[5] K.C. Wincewicz, J.S. Cooper, Taxonomies of SOFC material and manufacturing alternatives, J. Power Sources 140 (2005) 280–296, https://doi.org/10.1016/j.jpowsour.2004.08.032.

[6] Mixed-Ionic and Electronic Conduction and Stability of YSZ-Graphene Composites, accessed on 9 May 2025. Available online: https://colab.ws/articles/10.1016%2Fj.jeurceramsoc.2018.09.016.

[7] S. Ponnapureddy, A. Bhadauria, S. Bajpai, A. Tiwari, K.K. Pandey, A.K. Keshri, K. Balani, Enhanced reliability with bimodal microstructure and transformation-induced toughening in Al2O3-YSZ based thermal barrier coatings, Surf. Coat. Technol. 462 (2023) 129488, https://doi.org/10.1016/j.surfcoat.2023.129488.

[8] H. Guo, Y. Guo, Z. Xue, S. Gong, H. Xu, 1 - Overview of thermal barrier coatings for advanced gas turbine engine, in: H. Guo (Ed.), Thermal Barrier Coatings (Second Edition), Woodhead Publishing, 2023, pp. 1–20. Woodhead Publishing Series in Metals and Surface Engineering.

[9] K.R. Sridhar, J.A. Blanchard, Electronic conduction in low oxygen partial pressure measurements using an amperometric zirconia oxygen sensor, Sens. Actuators B Chem. 59 (1999) 60–67, https://doi.org/10.1016/S0925-4005(99)00233-6.

[10] M.N. Tsampas, F.M. Sapountzi, P. Vernoux, Applications of yttria stabilized zirconia (YSZ) in catalysis, Cat. Sci. Technol. 5 (2015) 4884–4900, https://doi.org/10.1039/C5CY00739A.

[11] Mineral Requirements for Clean Energy Transitions – The Role of Critical Minerals in Clean Energy Transitions – Analysis, accessed on 9 May 2025. Available online: https://www.iea.org/reports/the-role-of-critical-minerals-in-clean-energy-transitions/mineral-requirements-for-clean-energy-transitions.

[12] Recycling of Critical Minerals – Analysis, accessed on 6 March 2025. Available online: https://www.iea.org/reports/recycling-of-critical-minerals.

[13] S. Saffirio, S. Pylypko, S. Fiorot, I. Schiavi, S. Fiore, M. Santarelli, D. Ferrero, F. Smeacetto, S. Fiorilli, Hydrothermally-assisted recovery of yttria- stabilized zirconia (YSZ) from end-of-life solid oxide cells, Sustain. Mater. Technol. 33 (2022) e00473, https://doi.org/10.1016/j.susmat.2022.e00473.

[14] Yenesew, G.T.; Quarez, E.; Le gal la salle, A.; Nicollet, C.; Joubert, O. Recycling and characterization of end-of-life solid oxide fuel/Electrolyzer ceramic material cell components. Resour. Conserv. Recycl. 2023, 190, 106809, doi:https://doi.org/10.1016/j.resconrec.2022.106809.

[15] C. Kaiser, T. Buchwald, U.A. Peuker, Ultrasonic decoating as a new recycling path to separate oxygen side layers of solid oxide cells, Green Chem. 26 (2024) 960–967, https://doi.org/10.1039/D3GC03189F.

[16] S. Sarner, N.H. Menzler, A. Hilgers, O. Guillon, Recycling and reuse strategies for ceramic components of solid oxide cells, ECS Trans. 111 (2023) 1369, https://doi.org/10.1149/11106.1369ecst.

[17] S.H. Sarner, N. Menzler, J. Malzbender, M. Hilger, D. Sebold, A. Weber, O. Guillon, Towards a Scalable Recycling Process for Ceramics in Fuel-Electrode Supported Solid Oxide Cells vol. 27, Green Chemistry, 2025, pp. 2252–2262, https://doi.org/10.1039/D4GC05883F.

[18] V. Brard, O. Joubert, Le Gal La Salle, A., Development of multi-step acid/redox-based process for recovery of solid oxide cells components, Int. J. Hydrogen Energy 176 (2025) 150674, https://doi.org/10.1016/j.ijhydene.2025.150674.

[19] M. Kamiya, Y. Mori, T. Kojima, R. Sasai, H. Itoh, Recycling process for yttria-stabilized tetragonal zirconia ceramics using a hydrothermal treatment, J. Mater. Cycles Waste Manag. 9 (2007) 27–33, https://doi.org/10.1007/s10163-006-0168-3.

[20] S. Saffirio, S. Anelli, S. Pylypko, M.K. Rath, F. Smeacetto, S. Fiorilli, Recycling and reuse of ceramic materials from components of waste solid oxide cells (SOCs), Ceram. Int. 50 (2024) 34472–34477, https://doi.org/10.1016/j.ceramint.2024.06.206.

[21] H. Jiang, J. Li, Y. Xie, Y. Du, J. Zhao, Y. Mei, D. Xie, Rapid exfoliation and surface hydroxylation of high-quality boron nitride nanosheets enabling waterborne polyurethane with high thermal conductivity and flame retardancy, Adv. Compos. Hybrid Mater. 7 (2024) 8, https://doi.org/10.1007/s42114-023-00818-x.

[22] X. Ji, Y. Zhu, X. Lian, B. Fan, X. Liu, P. Xiao, Y. Zhang, Hydroxylation mechanism of phase regulation of nanocrystal BaTiO3 synthesized by a hydrothermal method, Ceram. Int. 48 (2022) 2281–2288, https://doi.org/10.1016/j.ceramint.2021.10.006.

[23] S. Sun, C. Li, Z. Sun, J. Wang, X. Wang, H. Ding, In-situ Design of Efficient Hydroxylated SiO2/g-C3N4 composite photocatalyst: synergistic effect of compounding and surface hydroxylation, Chem. Eng. J. 416 (2021) 129107, https://doi.org/10.1016/j.cej.2021.129107.

[24] M. Mori, J. Gramc, D. Hojkar, A. Lotric, F. Smeacetto, S. Fiorilli, S. Fiore, R. Stropnik, New life cycle inventories for end-of-life solid oxide cells based on novel recycling processes for critical solid oxide cell materials, Int. J. Hydrogen Energy 104 (2025) 635–650, https://doi.org/10.1016/j.ijhydene.2024.08.411.

[25] M. Bruno, S. Saffirio, F. Smeacetto, S. Fiorilli, S. Fiore, Optimising the selective leaching and recovery of cobalt, lanthanum, and strontium for recycling end-of-life solid oxide cells, Batteries 11 (2025) 124, https://doi.org/10.3390/batteries11040124.

[26] T. Babii, K. Jirátová, J. Balabánová, M. Koštejn, A. Michalcová, J. Maixner, F. Kovanda, Performance of nickel-manganese and nickel-cobalt-manganese mixed oxide catalysts in ethanol total oxidation, Catal. Today 428 (2024) 114438, https://doi.org/10.1016/j.cattod.2023.114438.

[27] F. Almomani, Ali H. Salah, M. Saad, Electrochemical oxidation of Ammonia (NH4+/NH3) ON synthesized nickel-cobalt oxide catalyst, Int. J. Hydrogen Energy 46 (2021) 4678–4690, https://doi.org/10.1016/j.ijhydene.2020.03.094.

[28] T. Fan, H. Liu, S. Shao, Y. Gong, G. Li, Z. Tang, Cobalt catalysts enable selective hydrogenation of CO2 toward diverse products: recent Progress and perspective, J. Phys. Chem. Lett. 12 (2021) 10486–10496, https://doi.org/10.1021/acs.jpclett.1c03043.

[29] C. Hernández Mejía, J.E.S. van der Hoeven, P.E. de Jongh, K.P. de Jong, Cobalt–Nickel nanoparticles supported on reducible oxides as fischer–tropsch catalysts, ACS Catal. 10 (2020) 7343–7354, https://doi.org/10.1021/acscatal.0c00777.

[30] M. Malik, K.H. Chan, G. Azimi, Review on the synthesis of LiNixMnyCo1-x-yO2 (NMC) cathodes for Lithium-ion batteries, Mater. Today Energy 28 (2022) 101066, https://doi.org/10.1016/j.mtener.2022.101066.

[31] G. Azimi, K.H. Chan, A review of contemporary and emerging recycling methods for Lithium-ion batteries with a focus on NMC cathodes, Resour. Conserv. Recycl. 209 (2024) 107825, https://doi.org/10.1016/j.resconrec.2024.107825.

[32] Nunes de Oliveira, A.M. Lima, D.C.R. Espinosa, A.B. Botelho Junior, J.A.S. Tenório, NCA-type Lithium-ion battery: A review of separation and purification technologies for Recycling Metals, J. Sustain. Metall 10 (2024) 1036–1050, https://doi.org/10.1007/s40831-024-00859-6.

[33] J.U. Choi, N. Voronina, Y. Sun, S. Myung, Recent Progress and perspective of advanced high-energy co-less Ni-rich cathodes for Li-ion batteries: yesterday, today, and tomorrow, Adv. Energy Mater. 10 (2020) 2002027, https://doi.org/10.1002/aenm.202002027.

[34] B. Jeevanantham, M.K. Shobana, Enhanced cathode materials for advanced Lithium-ion batteries using nickel-rich and Lithium/manganese-rich LiNi Mn Co O2, J. Energy Storage 54 (2022) 105353, https://doi.org/10.1016/j.est.2022.105353.

[35] A.R. Hanifi, M.A. Laguna-Bercero, N.K. Sandhu, T.H. Etsell, P. Sarkar, Tailoring the microstructure of a solid oxide fuel cell anode support by calcination and milling of YSZ, Sci. Rep. 6 (2016) 27359, https://doi.org/10.1038/srep27359.

[36] D. Mohanty, J.-Y. Hung, Y.-W. Chen, I.-M. Hung, Y.-R. Lin, Optimization and characterization of porous Ni/YSZ anode microstructure for solid oxide fuel cell, Ceram. Int. (2025), https://doi.org/10.1016/j.ceramint.2025.02.021.

[37] Y. Wang, M.E. Walter, K. Sabolsky, M.M. Seabaugh, Effects of powder sizes and reduction parameters on the strength of Ni–YSZ anodes, Solid State Ion. 177 (2006) 1517–1527, https://doi.org/10.1016/j.ssi.2006.07.010.

[38] P. Khajavi, P.V. Hendriksen, J. Chevalier, L. Gremillard, H.L. Frandsen, Improving the fracture toughness of stabilized zirconia-based solid oxide cells fuel electrode supports: effects of type and concentration of stabilizer(s), J. Eur. Ceram. Soc. 40 (2020) 5670–5682, https://doi.org/10.1016/j.jeurceramsoc.2020.05.042.

[39] O. Fakhraei, S. Hesaraki, M. Alizadeh, Evaluation of biphasic calcium phosphate/nanosized 3YSZ composites as toughened materials for bone substitution, Ceram. Int. 42 (2016) 11201–11208, https://doi.org/10.1016/j.ceramint.2016.04.030.
[40] G. Okuma, R. Usukawa, T. Osada, N. Kondo, H. Nakajima, T. Okazaki, S. Machida, Y. Arai, R. Inoue, H. Kakisawa, et al., Evolution of microstructure and defects in sintering of tape-cast alumina laminates observed by synchrotron X-ray multiscale tomography, Ceram. Int. 50 (2024) 37402–37411, https://doi.org/10.1016/j.ceramint.2024.04.096.
[41] B. Fang, J. Luo, New insights into the thermal aging mechanism of yttria stabilized zirconia: A phase field study, Ceram. Int. 48 (2022) 23365–23380, https://doi.org/10.1016/j.ceramint.2022.04.328.
[42] D. Marinha, M. Belmonte, Mixed-ionic and electronic conduction and stability of YSZ-graphene composites, J. Eur. Ceram. Soc. 39 (2019) 389–395, https://doi.org/10.1016/j.jeurceramsoc.2018.09.016.
[43] M. Jovaní, H. Beltrán-Mir, E. Cordoncillo, A.R. West, Atmosphere- and voltage-dependent electronic conductivity of oxide-ion-conducting Zr1–xYxO2–x/2 ceramics, Inorg. Chem. 56 (2017) 7081–7088, https://doi.org/10.1021/acs.inorgchem.7b00673.
[44] Field-Induced p-n Transition in Yttria-Stabilized Zirconia | Scientific Reports, accessed on 9 May 2025. Available online: https://www.nature.com/articles/s41598-019-54588-y.
[45] M. Alotaibi, L. Li, R. West, A. Electrical properties of yttria-stabilised Hafnia ceramics, Phys. Chem. Chem. Phys. 23 (2021) 25951–25960, https://doi.org/10.1039/D1CP04642J.
[46] N.M. Sammes, Z. Cai, Ionic conductivity of ceria/yttria stabilized zirconia electrolyte materials, Solid State Ion. 100 (1997) 39–44, https://doi.org/10.1016/S0167-2738(97)00306-8.
[47] J. Lee, Electrical conductivity and defect structure of yttria-doped ceria-stabilized zirconia, Solid State Ion. 144 (2001) 175–184, https://doi.org/10.1016/S0167-2738(01)00903-1.